Matter

Article

Giant berry curvature in amorphous ferromagnet Co_2MnGa

Graphical abstract

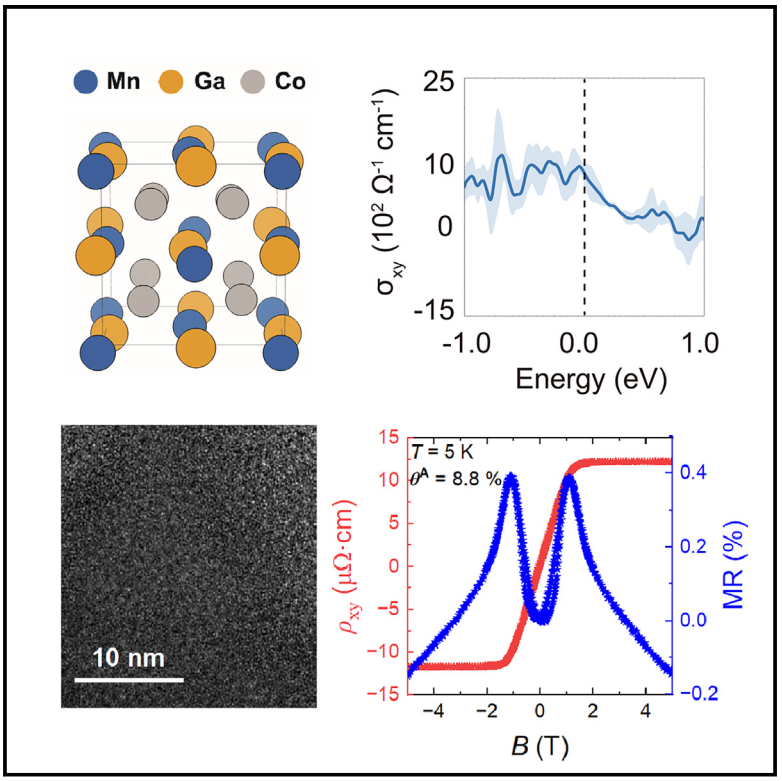

Highlights

- Giant anomalous Hall conductivity is found in a highly disordered topological ferromagnet
- Amorphous and highly ordered Co_2MnGa share similar ferromagnetic interactions
- The topology of the electronic bands is sensitive to the local chemical structures

Authors

Weiyao Zhao, Yao Zhang, Yuefeng Yin, ..., Nikhil V. Medkehar, Simon Granville, Julie Karel

Correspondence

julie.karel@monash.edu

In brief

In this study, we present a low-cost, industry-compatible method for fabricating amorphous ferromagnetic thin films for future electronic applications. Remarkably, these highly disordered films exhibit similarities to the chemically and structurally ordered Co_2MnGa, including its topological electronic structures. This advancement, which features lower energy consumption, has the potential to significantly simplify the manufacturing process of magnetic memory devices. Our findings open an alternative pathway to accelerate the practical adoption of topological materials in real-world applications.

Zhao et al., 2025, Matter *8*, 101988
March 5, 2025
https://doi.org/10.1016/j.matt.2025.101988

1 Discovery
A new material or phenomena

CellPress

Matter

CellPress

Article

Giant berry curvature in amorphous ferromagnet Co_2MnGa

Weiyao Zhao,[1,2,11] Yao Zhang,[3,11] Yuefeng Yin,[1,2,11] Kaijian Xing,[4] Shengqiang Zhou,[5] Abdulhakim Bake,[6] Golrokh Akhgar,[1,2,7] David Cortie,[8] Lei Chen,[9] Xiaolin Wang,[6] Kirrily C. Rule,[8] Nikhil V. Medkehar,[1,2] Simon Granville,[3,10] and Julie Karel[1,2,12,*]

[1]Department of Materials Science & Engineering, Monash University, Clayton, VIC 3800, Australia
[2]ARC Centre of Excellence in Future Low-Energy Electronics Technologies, Monash University, Clayton, VIC 3800, Australia
[3]Robinson Research Institute, Victoria University of Wellington, Wellington, New Zealand
[4]School of Physics & Astronomy, Monash University, Clayton, VIC 3800, Australia
[5]Helmholtz-Zentrum Dresden-Rossendorf, Institute of Ion Beam Physics and Materials Research, Bautzner Landstr. 400, 01328 Dresden, Germany
[6]Institute for Superconducting & Electronic Materials, University of Wollongong, North Wollongong, NSW 2500, Australia
[7]Manufacturing, CSIRO, Linfield, NSW 2070, Australia
[8]Australian Nuclear Science and Technology Organisation, Lucas Heights, NSW 2234, Australia
[9]Centre for Future Materials, University of Southern Queensland, Springfield, QLD 4300, Australia
[10]MacDiarmid Institute for Advanced Materials and Nanotechnology, Wellington 6011, New Zealand
[11]These authors contributed equally
[12]Lead contact
*Correspondence: julie.karel@monash.edu
https://doi.org/10.1016/j.matt.2025.101988

PROGRESS AND POTENTIAL Magnetic random-access memory is one of the most promising next-generation data storage technologies, offering unique advantages in high-value application scenarios. Co_2MnGa, a well-known magnetic Weyl semimetal, holds significant potential for spintronic applications due to its giant intrinsic anomalous Hall effect. Previous studies have primarily focused on crystalline Co_2MnGa, revealing that increased chemical disorder in the lattice (e.g., transitioning from the $L2_1$ to B2 structure) leads to a reduced magnetic moment and anomalous Hall effect. Consequently, one might expect that an amorphous material, characterized by chemical and structural disorder, would exhibit a significantly diminished anomalous Hall effect due to near-zero Berry curvature. Remarkably, our study demonstrates the opposite: amorphous Co_2MnGa thin films exhibit a large anomalous Hall effect and anomalous Hall angle at room temperature, driven by the Berry curvature. Elastic neutron scattering and density functional theory calculations suggest that the local atomic environment in amorphous Co_2MnGa closely resembles that of the chemically ordered $L2_1$ structure despite the absence of long-range order. This local structural similarity is responsible for the Berry curvature and the resulting anomalous Hall properties.
Our findings represent the first demonstration of an amorphous magnetic Weyl semimetal, highlighting its potential for spintronic and caloritronic applications. Furthermore, this work suggests a broader opportunity to develop other amorphous magnetic quantum materials where topological features in the electronic structure are preserved despite the lack of long-range order.

SUMMARY

In amorphous materials, long-range translational order breaks down, and k is no longer a good quantum number; however, some of the phenomena, for instance ferromagnetic interactions and a mechanism similar to the Berry curvature, can be preserved. Here, we demonstrate a giant Berry-curvature-induced anomalous Hall effect and anomalous Hall angle in amorphous Co_2MnGa (a-CMG) thin films. Remarkably, the effect presents the same magnitude as high-quality crystalline CMG with the $L2_1$ structure. The elastic neutron scattering peak in a-CMG is centered close to the crystalline phase, indicating that the amorphous material presents similar local atomic environments and magnetic interactions. First-principles density functional theory calculations further show that the anomalous Hall conductivity arises only when the local environments in the amorphous structure are similar to the $L2_1$ phase. Our work strongly points to the application of low-cost,

industry-compatible, and thermally stable amorphous topological materials in emerging electronic and spintronic applications.

INTRODUCTION

The anomalous Hall effect (AHE), characterized by a transverse electric current, can have intrinsic and extrinsic origins and is vital in modern spintronic devices, such as Hall sensors. The intrinsic contribution to the AHE that is governed by the quantum geometry of the electronic Bloch bands, e.g., the non-vanishing Berry curvature, has recently been discovered in numerous magnetic materials.[1–6] These nontrivial electronic states are well defined and understood in single crystals with low defect density, although epitaxial (single-crystal) films present practical challenges upon implementation in integrated circuit applications, where disorder is difficult to completely eliminate. By contrast, amorphous materials offer a unique prospect in future electronic and spintronic devices; they are low cost and defect tolerant and require less energy to synthesize than single-crystal thin films. Despite the potential advantages, these materials are generally overlooked in electronic devices because of the expectation that disorder modifies the physical properties of the material, thereby reducing performance. While the reciprocal space vector k in highly disordered materials is not well defined, magnetism can be robust to disorder. Although the long-range translational symmetry is absent in these materials, local atomic environments resembling the crystalline material can be preserved.[7,8] Such a similarity in the local environments between an amorphous and crystalline material suggests that the magnetic and electronic properties of the material, which are often dictated by local interactions and symmetries, can also be similar.

Indeed, numerous examples exist where the magnetic properties of the crystalline material are preserved in the amorphous system. For instance, amorphous FeGe thin films exhibit chiral spin textures,[9] analogous to the crystalline B20 compound FeGe, which is a chiral magnet with a screw spin structure. Additionally, both crystalline and amorphous FeGe host skyrmions—specifically a skyrmion lattice near room temperature[10] in the former and isolated antiskyrmions and skyrmions in the latter. This work is strong evidence that the local atomic structure and spin interactions are similar to those of the crystalline form from the perspective of real-space topology.

Moreover, recent theoretical predictions suggest that liquid-like networks also support chiral edge modes in the absence of long-range spatial order.[11] This finding indicates that, similar to the real-space case, the topological feature is also preserved in reciprocal space, and the nontrivial boundary modes can be protected by the local symmetry. Although the Berry phase, which relies on the integral over the whole Brillouin zone, does not exist, a short-range atomic-structure-related Berry curvature can still be defined. This Berry curvature can be estimated and was found to result in a large anomalous Hall angle in amorphous $Fe_{1-x}Ge_x$ films.[12,13] Recently, a large AHE in amorphous $Fe_{1-x}Sn_x$ thin films was also found, where the local kagome-like fragments embedded in the amorphous matrix on the length scale of a few nanometers play a key role.[14]

Our methodology in this work, therefore, is to identify potential *topological* performance in an amorphous compound by considering the properties of the crystalline analog. For example, B20 compounds such as CoSi, CoGe, RhSi, and RhGe are known for presenting multiple types of topological fermions.[15–17] In the amorphous state, a large anomalous Hall angle induced by a large Berry curvature was also observed.[12,18] Thus, we aim to search for a high-performance amorphous magnet among high Curie temperature (T_C) ferromagnets with exotic electronic band structures. A well-known topological material with these properties is Co_2MnGa (CMG), which has been confirmed as a topological Weyl nodal-line semimetal by angular resolved photoemission spectroscopy (ARPES).[19] The Weyl nodal line in CMG sits close to the Fermi level, inducing a giant Berry curvature in this system, and thus contributing to a giant anomalous Nernst effect[20] and giant AHE[21] in single crystals. High quality epitaxial thin films show similar effects,[22] including a thickness-dependent Berry curvature modulation.[23,24] A sizable spin-orbit torque effect was also observed in epitaxial CMG films, indicating potential in magnetic random-access memory technology.[25–28] Polycrystalline CMG films have shown a substantial anomalous Nernst effect,[29,30] highlighting the potential for retaining the large Berry curvature in this material even with substantial disorder.

In this work, we will show that the ferromagnetism and related topological properties are preserved in amorphous CMG (a-CMG). We report a large AHE and anomalous Hall angle and strong magnetic exchange interactions. The elastic neutron scattering experiments confirm that the ferromagnetic interaction is strong over a large range of Mn-Mn interatomic distances, which are centered around the crystalline Mn-Mn interatomic distance. This result points to the finite disorder model in a-CMG films, meaning that these films exhibit crystalline-like short-range atomic bonding order (Figure 1A, inset). The crystalline-like magnetic interactions contribute to a large Berry curvature, as well as the anomalous Hall response. First-principles density functional theory (DFT) simulations using the finite disorder model further support a large anomalous Hall conductivity in a-CMG only when the local atomic environments are similar to the $L2_1$ structure. Notably, these effects remain dominant in the transport behavior at room temperature. This work points toward an amorphous magnetic Weyl semimetal with great potential in spintronics applications.

RESULTS

AHE in a-CMG thin films

Thin films of CMG (S_1: 50 nm and S_2: 1,000 nm) were deposited on amorphous SiO_2/Si substrates at room temperature (see the methods section for details).[9,12–14,18,31] X-ray diffraction (XRD) patterns of the as-grown thin films are shown in Figure 1A; no clear CMG peaks are present in either sample. Note that the only difference between samples S_1 and S_2 is the thickness. S_1 is used for electronic transport measurements and polarized

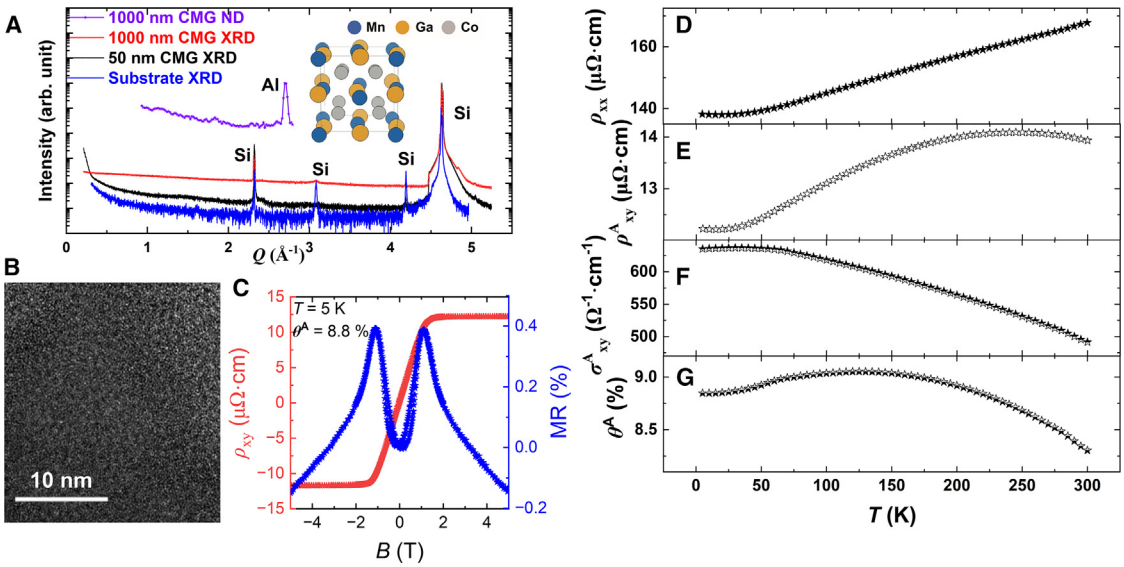

Figure 1. Structural and electronic transport properties of a-CMG films

(A) XRD and elastic neutron scattering patterns of a-CMG films.

(B) The cross-section TEM image of S_2.

(C) The magnetoresistance and Hall effect of an a-CMG Hall bar at 5 K.

(D–G) The longitudinal resistivity, anomalous Hall resistivity, anomalous Hall conductivity, and anomalous Hall angle measured in an a-CMG Hall bar in 5–300 K range.

neutron reflectivity measurements and S_2 for the elastic neutron scattering measurements. To compare with the neutron diffraction patterns obtained from Taipan (wave length $\lambda_N = 2.345$ Å), all diffraction data are converted to counts (intensity) versus Q in Figure 1A. The films are aligned nearly perfectly during XRD measurements, which is evidenced by the dynamic diffraction peaks of the Si substrate. The peak-less feature from the XRD patterns suggests that these a-CMG films do not exhibit long-range order. To verify the amorphous structure, cross-sectional high-resolution transmission electron microscopy (TEM) was conducted on S_2 using a lamella prepared with a focused ion beam lift-out technique (Figures 1B and S1). As shown in Figure S1, the thin-film thickness (~960 nm) of S_2 is very close to the target value (1,000 nm), and the a-SiO_x (~100 nm thick on top of the (0001)-oriented silicon wafer) exhibits a sharp and flat interface with the a-CMG film. Figure 1B shows a high-magnification image of the a-CMG film where the amorphous features can be observed. Additional cross-sectional TEM images, as well as a fast Fourier transform (FFT) pattern of the high-magnification image, are presented in Figure S1. The broad diffuse ring feature in the FFT pattern further verifies the amorphous state of the sample. Some lattice fringes and nanocrystals were found, comprising less than about 15% volume fraction; such a small volume fraction is not expected to dominate the transport behavior.

To study the electronic transport properties of a-CMG, we fabricated a Hall-bar-shaped device on sample S_1 and conducted magnetotransport measurements over a wide temperature region (see methods for details). As shown in Figure 1C, at low temperatures, a large AHE and butterfly-shaped magnetoresistance (MR) are observed, similar to previous studies of epitaxial CMG films.[23] The MR has positive and negative components, which suggests multiple contributions from the AHE,[32] and possible electron-magnon scattering.[33] These observations suggest that the a-CMG films are still ferromagnetically ordered, a point that is further confirmed via polarized neutron reflectivity measurements (see the supplemental information for details). Similar transport features, e.g., the coupled AHE and crossover between positive and negative MR, are also observed in sample S_1, as shown in Figure S2. The temperature-dependent measurements of both the longitudinal and transverse resistivity are also shown in Figures 1D and 1E, respectively. The anomalous Hall conductivity and anomalous Hall angle ($\theta^A = \sigma^A_{xy}/\sigma_{xx}$; more data processing details are in the methods section) are calculated and plotted in Figures 1F and 1G. The anomalous Hall conductivities for a-CMG are ~635 Ω^{-1}cm^{-1} at 5 K and ~488 Ω^{-1}cm^{-1} at 300 K, which are smaller than the maximum reports in single crystals (~1,160 Ω^{-1}cm^{-1} in 2–250 K range)[21] and epitaxial films (~800 Ω^{-1}cm^{-1} at 2 K).[23] The anomalous Hall angle in a-CMG is ~8.2% at room temperature, which is slightly smaller than those reported in single crystals (12%)[21] and epitaxial films (11.2%).[23] The a-CMG possesses a much larger anomalous angle than most previously reported amorphous or crystalline quantum materials.[12] These results suggest that the magnetic ordering in a-CMG may play an important role in its electronic structure and transport behavior.

Magnetic properties

We therefore employ magnetometry and elastic neutron scattering measurements to probe the magnetic properties in a-CMG. In the crystalline Heusler compounds X_2YZ, the atoms

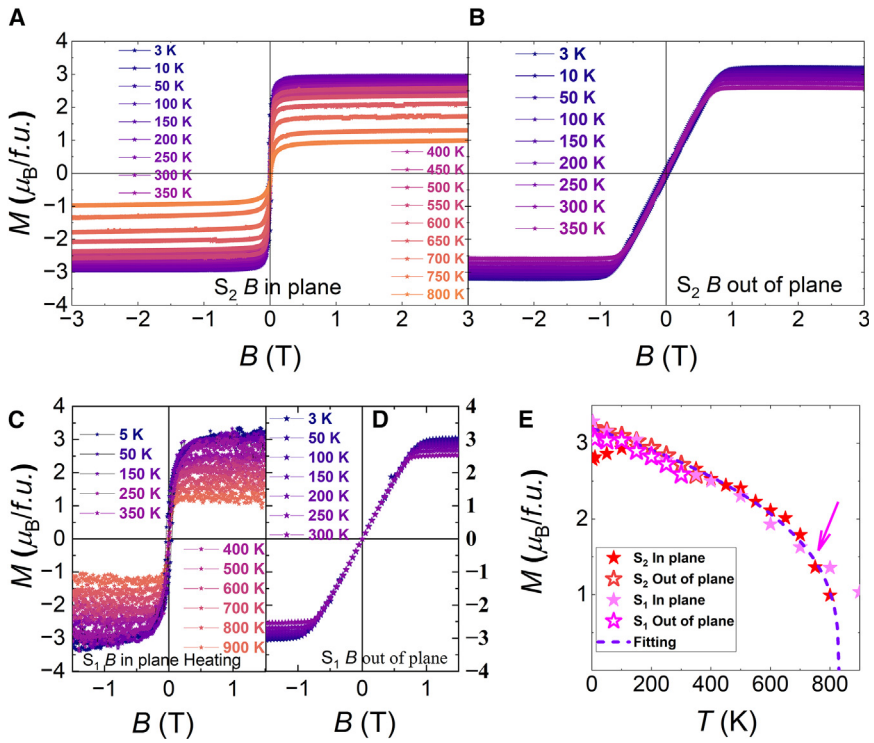

Figure 2. The magnetic properties of a-CMG films

(A and B) The MH curves of S_2 in 3–800 K region, with the magnetic field applied in the thin-film plane (A); the out-of-plane measurements in the 3–350 K region are shown in (B).

(C and D) S_1 in-plane MH curves for 5–900 K (C) and out-of-plane curves for 3–300 K (D) measured while heating.

(E) The saturated magnetizations in (A)–(D) are summarized as a function of temperature.

Note that the arrow in (E) indicates the crystallization point.

crystallize in an ordered structure belonging to either the $Fm\bar{3}m$ or $F\bar{4}3m$ space group.[34] The magnetic structure and Berry curvature are sensitive to the distances among magnetic elements, as well as the symmetry,[21] while in the amorphous system, the situation can be more complicated, e.g., the translational symmetry is broken, and the distance among magnetic elements exhibits a distribution.

Figure 2 show the temperature dependence of the field-dependent magnetization (magnetic hysteresis [MH]) curves with a magnetic field applied in the thin-film plane and along the normal direction, respectively, for S_2 (Figures 2A and 2B) and S_1 (Figures 2C and 2D). For both samples, the magnetic anisotropy evident upon comparison of the two orientations of the applied magnetic field originates from shape anisotropy; the magnetization favors the in-plane direction. This result is consistent with other amorphous 3*d* transition metal thin films.[12,35,36] In-plane magnetic anisotropy has also been reported in (relatively) thick crystalline/epitaxial CMG films.[23] However, the saturation moment (~3 μ_B/f.u.) is significantly smaller than that in epitaxial films and single crystals (4.1 μ_B/f.u.).[37] With heating, the in-plane and out-of-plane saturation magnetizations behave slightly differently below 100 K, as shown in Figure 2D. However, above 125 K, the magnetization coincides for both the in-plane and out-of-plane configurations. Only the in-plane configuration is available in the high-temperature region due to the sample mounting method. The magnetization of both samples can be fitted with $M(T) = M_s \cdot (1 - T/T_C)^{\beta}$, where M_s is the saturation magnetization and β = ~0.34 for transition metals. The obtained T_c for the a-CMG is ~830 K, higher than the ordering temperature in crystalline CMG. Moreover, upon heating, the a-CMG films are stable up to at least 600 K (Figures S4 and S5), which is higher than typical back-end-of-line processes in advanced CMOS technologies.[38–40]

Sample S_1 (50 nm) was further heated to 900 K; Figure 2D reveals that the saturation moment disagrees with the fitting curve at both 800 and 900 K. Cooling measurements from 900 to 350 K show a significant increase in the saturation moment after the *in situ* heat treatment (Figure S4), as has been seen before in CMG films deposited on non-crystalline substrates.[41] When extrapolated to 0 K, this results in a similar saturation magnetization (4.3 μ_B/f.u.) to crystalline CMG. The magnetic moments of Co and Mn in crystalline CMG are ~0.75 and 2.78 μ_B,[42] respectively. The magnetization in a-CMG prior to heating to 900 K likely arises mainly from the Mn moments. The vanishing Co moment behavior has also been reported in the high-temperature paramagnetic phase of CMG.[37] In amorphous Co_xSi_{1-x} or Co_xGe_{1-x}, the onset of ferromagnetism occurs at x = 0.6,[12] which is relatively high in comparison to amorphous Fe_xSi_{1-x} or Fe_xGe_{1-x}, where ferromagnetism appears near x = ~0.40. These factors suggest that the Co magnetic moment may be reduced in a-CMG due to the relatively low concentration (~50%) and disorder. It is speculated that, after the heat treatment, the Co atoms in the crystallized CMG gain a moment and, therefore, the material presents a larger M_s in the cooling sweep.

Elastic neutron scattering

Figure 3A shows the elastic neutron scattering intensity versus *Q*, and the details of the experimental setup and data processing can be found in the methods section and the supplemental information. At 25 K, a broadened peak in the 0.8–2.0 $Å^{-1}$ range with some features can be resolved. The overall intensity drops when heating to 750 K, which is slightly below the T_c obtained from the magnetization measurements. However, some of the features, e.g., the peaks at *Q* = 1.34, 1.74, and 1.99 $Å^{-1}$ (or *d* = 4.69, 3.61, and 3.16 Å), gain intensity during heating above ~650 K and are sharper at high temperatures. These peaks indicate the partial crystallization of the material at high temperatures. The major peak at 1.16 $Å^{-1}$ (*d* spacing = 5.42 Å) is close to the lattice constant (second nearest-neighbor Mn-Mn pairs) of crystalline CMG (5.77 Å), while the other broadened peak at 1.58 $Å^{-1}$

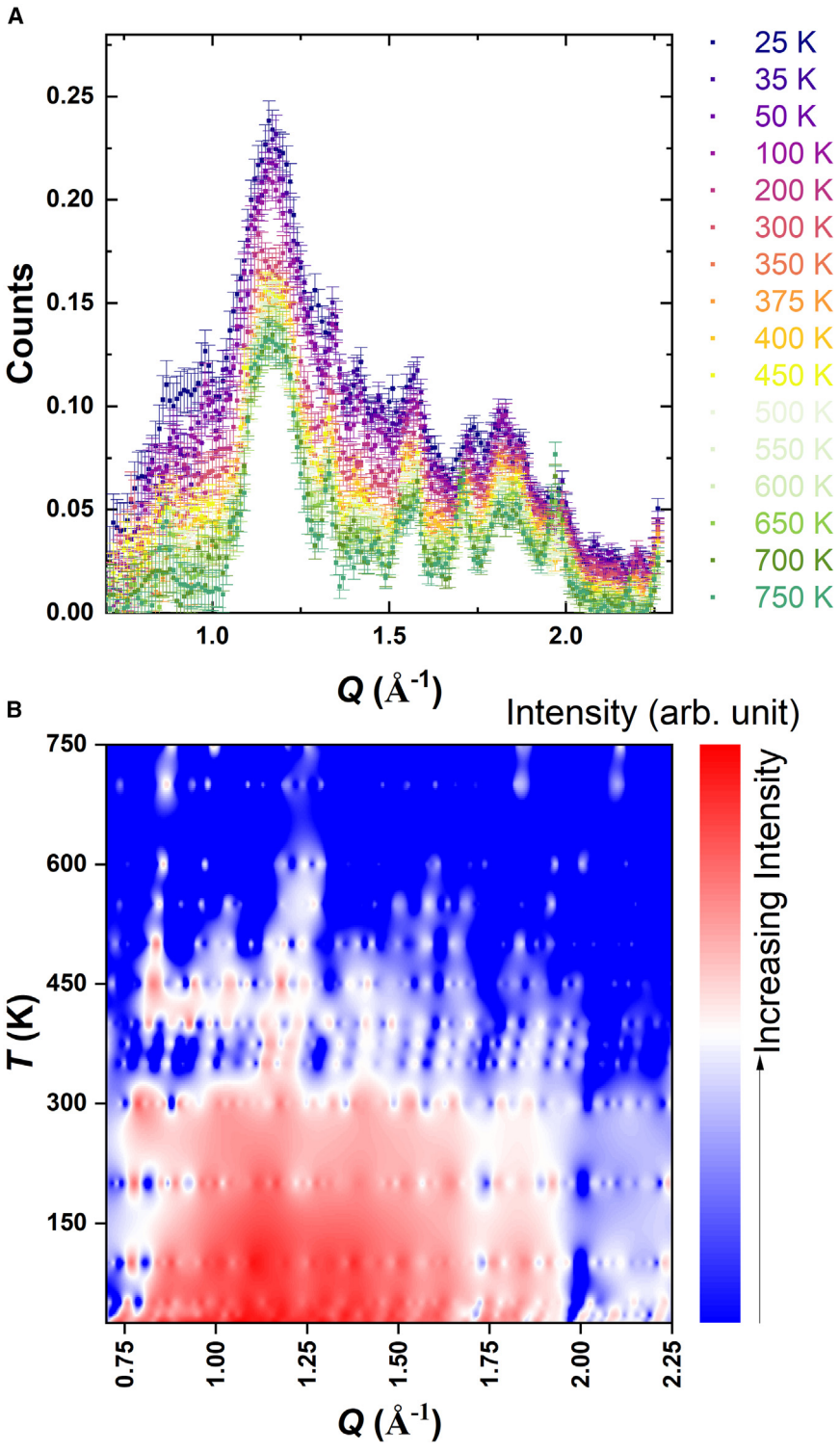

Figure 3. Elastic neutron scattering measurements

(A) The temperature-dependent scattering intensity with *Q*. Measurement error bars are shown for each data point.

(B) Background-subtracted scattering results.

(*d* spacing = 3.98 Å) is close to the nearest-neighbor Mn-Mn bond (4.08 Å). One may assume that the magnetic scattering intensity at 750 K is near zero. Therefore, by subtracting the scattering curve at 750 K, the magnetic scattering signal can be isolated, as shown in Figure 3B (see also Figure S3). The strongest feature between 0.8 and 1.7 $Å^{-1}$ below ~450 K indicates the ferromagnetic interaction is (mainly) between Mn-Mn pairs. The elastic neutron scattering results suggest that the a-CMG possesses crystalline CMG-like atomic environments. The finite disorder of the atomic arrangements in a-CMG still preserves critical features such as strong ferromagnetic ordering among Mn atoms with interatomic distances similar to crystalline CMG. This local atomic environment may be the reason for the observed giant AHE in a-CMG.

Calculations of the giant anomalous Hall conductivity

First-principles DFT calculations were performed to gain more insight into the large AHE measured in a-CMG. Different degrees of random atomic perturbations were applied to pristine (crystalline $L2_1$) CMG as shown in Figure 4A. In the pristine+displacements scenario, the pristine bonding order is maintained with only small atomic oscillations applied. In the B2+displacements scenario, the B2 phase (Mn and Ga occupation assigned randomly) is used as the starting point, and the Mn/Ga bonding is disrupted. Finally, a random lattice where only the number of atoms from the pristine CMG is conserved was also considered. In this configuration, the pristine atomic environments are no longer preserved. A similar disordered structure can be obtained by using a "melt-and-quench" *ab initio* molecular dynamic (AIMD) process on the B2 phase (B2+displacements+AIMD).

Figures 4B and 4C show that the anomalous Hall conductivity (AHC) at the Fermi level drastically decreases for all cases except the pristine+displacements configuration. In the randomly generated lattice, the AHC curve becomes nearly featureless, without any identifiable pristine remnants. In the pristine+displacements configuration, a considerable AHC (67.6% of the pristine, 881 $\Omega^{-1}cm^{-1}$) is still observed at the Fermi level and conforms to the pristine character. This correlation aligns well with experimental trends and suggests that a-CMG's significant AHC

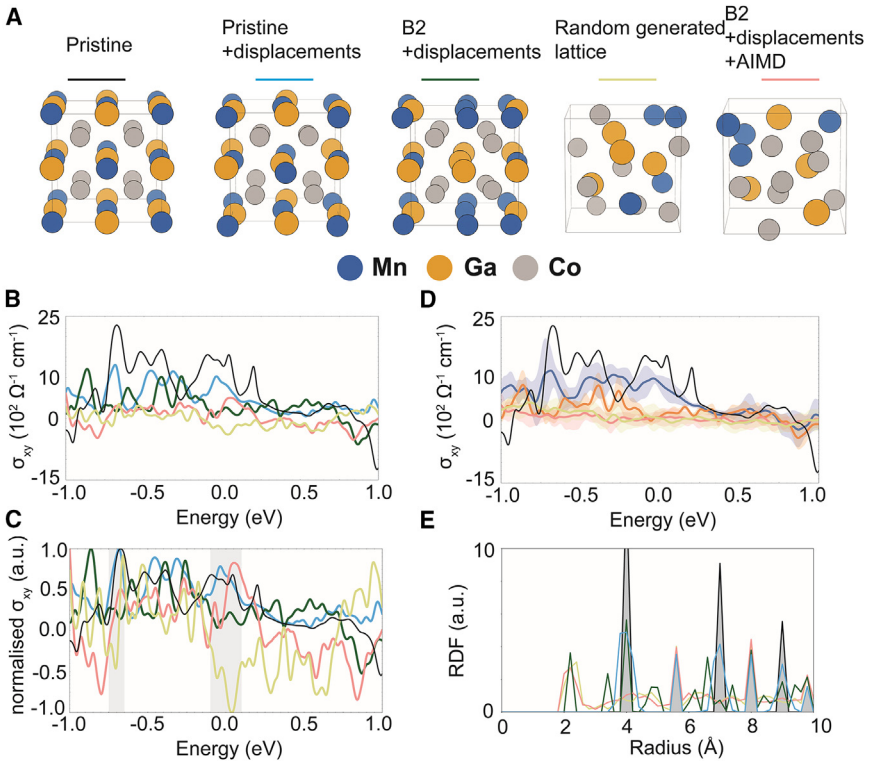

Figure 4. Understanding the impact of atomic order on the anomalous Hall conductivity of CMG

(A) Different atomic configurations considered with different degrees of disruptions to pristine ($L2_1$) bonds. See the main text for details.

(B) AHC for the configurations described in (A). The color for each configuration is shown under the text in (A).

(C) Normalized anomalous Hall conductivity (AHC) for the configurations present in (A) to highlight the position of peaks in (B). The areas where traces of pristine AHC are clearly visible in the pristine+displacements configuration are highlighted in gray shades. The normalized AHC is obtained by scaling the original AHC value to the maximum AHC value for each case. Therefore, the normalized AHC value falls within the range of −1 to 1.

(D) AHC calculated by statistically averaging 12 randomly initialized cases for each configuration with disruptions. The standard deviation of the data is shown as the shaded area around the averaged line.

(E) Radial distribution function (RDF) of Mn-Mn bonds for each disrupted configuration, with the pristine RDF shown in the background in gray shades.

originates from the presence of local atomic environments, which resemble pristine-ordered (e.g., crystalline $L2_1$) CMG. This claim can be further demonstrated in the statistically averaged AHC over 12 cases for each scenario shown in Figure 4D. The AHC determined from the randomly generated lattice is nearly zero, while the pristine+displacements configuration maintains the characteristic peaks and high AHC. The changes in the local atomic environments can be further examined in the calculated radial distribution function (RDF) shown in Figure 4E. Specifically, these data show changes in bond distribution as a function of distance for Mn-Mn pairs for the different perturbation scenarios. The short Mn-Mn bonds (less than 3 Å) occupy a significant fraction of the bonds in the B2-based and randomly generated lattices. This deviation from the pristine bond order may be the reason for the nearly zero AHC found in Figure 4D in the B2-based and random lattices.

DISCUSSION

The DFT results suggest that a-CMG on the local level is more reminiscent of the chemically and structurally ordered $L2_1$ phase than the more disordered structures. This is an incredibly surprising result and, more importantly, has practical implications in advanced electronic manufacturing. Thin-film growth to obtain the $L2_1$ structure generally requires a single-crystal substrate, elevated growth temperatures, and careful control over the growth parameters. Without these factors, the disordered B2 structure is more likely to appear. Our work has shown that thin-film growth at room temperature on an amorphous substrate results in a material that, remarkably, is reminiscent of the $L2_1$ phase and presents a large AHE and anomalous Hall angle. This work suggests that other crystalline topological 3*d* transition metal compounds, such as noncolinear Mn-based antiferromagnets, are possible candidates for locating amorphous films with large Berry curvature. These materials could also be used in magnetic tunnel junction design,[43] which would further reduce the technical barrier and manufacturing cost for next-generation spintronic devices.

To summarize, the magnetic and electronic properties of a-CMG thin films were studied. Magnetometry revealed a saturation moment of ~3.2 μ_B/f.u., which is smaller than the crystalline phase and can be understood by the ferromagnetic ordering among Mn atoms and the reduction in the Co moment. The strong Mn-Mn ferromagnetic interactions are further demonstrated by the elastic neutron scattering peak between 0.8 and 1.7 $Å^{-1}$ below ~450 K. It is worth mentioning that the peak features in neutron scattering suggest that the Mn atoms exhibit local atomic structures similar to the crystalline material, which possesses a large Berry-curvature-induced anomalous Hall conductivity. Moreover, DFT results reveal that a large AHC is only preserved in simulated structures where the local atomic environments are similar to crystalline $L2_1$ CMG. Therefore, we deduce that the local order and ferromagnetism of Mn atoms with finite disorder in a-CMG contribute to the large anomalous Hall conductivity and giant anomalous Hall angle at room temperature. This result is consistent with previous work on crystalline Mn-based Heusler materials[44] that has shown that the local Mn environment can drastically affect the magnetic and electronic properties of the material. Our study yielded a low-cost, facile synthesis of a-CMG, with properties reminiscent of the nodal line Weyl semimetal crystalline analog. This methodology

can perhaps be extended to other Mn-based quantum materials to realize novel amorphous systems for emerging electronic and spintronic applications at room temperature.

METHODS

Thin-film deposition

The thin films of CMG (50 and 1,000 nm, S_1 and S_2) were deposited on 4 inch SiO_x(100 nm)/Si substrates in a Kurt J. Lesker CMS-18 magnetron sputtering system with a base pressure below 3×10^{-8} Torr. The thin films were DC magnetron sputtered from a stoichiometric polycrystalline target at 100 W under 6 mTorr of Ar. A 3 nm Ta capping layer was then deposited on the film. The Ta oxidizes to form an ~4 nm native oxide film, which will not contribute to the transport behavior. The XRD measurements were conducted using a Rikagu Smartlab diffractometer with Cu K_α radiation. Cross-section TEM was employed to characterize the nanostructure of the thin film. The lamella was prepared using the focused ion beam lift-off technique on sample S_2.

Elastic neutron scattering measurements

A triple-axis neutron spectrometer in ANSTO using a thermal neutron source, Taipan, was employed to measure the elastic scattering from the a-CMG sample. Taipan was aligned with a fixed final energy of 14.87 meV and 0-40'-40'-0 collimation for high Q-resolution with a vertically focused monochromator to improve intensity. A graphite filter was utilized on the scattered arm to remove higher-order scattering. The top-loaded cryostat with a temperature range of 5–800 K was employed to provide the temperature-dependent sample environment.

Magnetic and transport properties

The magnetization as a function of temperature and magnetic field was measured using the vibration sample magnetometer (VSM) equipped on a physical property measurement system (PPMS; Quantum Design DynaCool-9). A heating stick was employed in the oven mode to support MH measurements up to 900 K. The electronic transport measurements were conducted using the electronic transport measurement function in PPMS. A standard Hall bar structure (50 × 500 μm) was patterned on the thin film using standard optical lithography and Ar milling for the transport measurements. From the AHE curve of both samples, it could be expected that the anomalous Hall resistivity saturated above ~1.1 T; therefore, we used the large-field value $\rho_{xy}^A = \rho_{xy}^A(3.5\ \mathrm{T})$ and then employ the conductivity tensor to calculate the anomalous Hall conductivity: $\sigma_{xy}^A = \frac{\rho_{xy}^A}{\rho_{xy}^2+\rho_{xx}^2}$.

DFT calculation details

We used DFT calculations as implemented in the Vienna Ab initio Simulation Package (VASP) to calculate the electronic structure of CMG.[45] The Perdew-Burke-Ernzehof (PBE) form of the generalized gradient approximation (GGA) was used to describe electron exchange and correlation.[46] The kinetic energy cutoff for the plane-wave basis was set to 400 eV. We used a 12 × 12 × 12 Γ-centered k-point mesh for sampling the Brillouin zone. The spin-orbit interaction was included in the calculations. For the calculation of anomalous Hall conductivity of CMG, we adopted the method as implemented in the open-source code WannierTools,[47,48] which uses the standard Kubo formula,[49,50] based on the Wannier tight-binding Hamiltonian obtained from wannier90.[51] Co/Mn d and Ga s p orbitals are used as projectors for tight-binding Hamiltonian construction.

For the investigation of the bonding environment in a-CMG, we introduced random displacements to the atomic positions of the crystalline lattice as follows.

(1) For the B2 lattice, we randomly swapped pristine Mn and Ga sites to create the B2-like configuration.
(2) For pristine+displacements and B2+displacements configurations, we applied random displacements ranging from −0.2 to 0.2 Å in all three Cartesian directions relative to the atomic positions in the pristine configuration for all atoms.
(3) For random-generated lattices, we initialize Co/Mn/Ga atom positions in randomly generated fractional coordinates within the pristine lattice. Each atom's position and element species were initialized randomly, while an algorithm ensured that newly added atoms met the minimum bonding distance based on the covalent radii of each element. If a newly added atom was found to be smaller than the minimum bonding distance to an existing atom, then its entry would be rejected, and new random coordinates and species were selected. This process continued until the Co/Mn/Ga atom count matched that of the pristine lattice.

These altered lattice configurations were then relaxed using DFT until all atomic forces were reduced to below 0.01 eV. To further alter the bonding order, we also perform melt-and-quench AIMD simulations. The structure was melted at 3,000 K for 3 ps and then quenched to the ground state at a rate of 1 K/fs. The cell volume was fixed during the MD simulations.

We generated 12 random cases for each type of crystal perturbation considered, enabling us to calculate a statistically averaged anomalous Hall conductivity curve that demonstrates how the disruption of pristine bonds influences transport measurements.

RESOURCE AVAILABILITY

Lead contact

Further information and requests for resources should be directed to the lead contact, Dr. Julie Karel (julie.karel@monash.edu).

Materials availability

The materials generated in this study may be made available upon request.

Data and code availability

The data that support the findings of this study are available from the corresponding author upon request.

ACKNOWLEDGMENTS

This work is supported by ARC Centre of Excellence in Future Low-Energy Electronics Technologies no. CE170100039 and Australian Research Council Discovery Projects DP200102477 and DP220103783. The beamtime from ANSTO, P15684 on Platypus and P15648 on Taipan, is acknowledged. W.Z.

acknowledges the support from AINSE through ECRG. Y.Y. and N.V.M. gratefully acknowledge computational support from the NCI National Facility at the Australian National University and Pawsey Supercomputing facility. This work was performed in part at the Melbourne Center for Nanofabrication (MCN) in the Victorian Node of the Australian National Fabrication Facility (ANFF). The MacDiarmid Institute is supported under the New Zealand Centres of Research Excellence Programme.

AUTHOR CONTRIBUTIONS

Conceptualization, W.Z. and J.K.; methodology, W.Z., Y.Z., and Y.Y.; investigation, W.Z., Y.Z., Y.Y., K.X., S.Z., A.B., G.A., D.C., L.C., X.W., and K.C.R.; writing – original draft, W.Z. and Y.Y.; writing – review and editing, Y.Z., S.G., and J.K.; funding acquisition, J.K.; supervision, N.V.M., S.G., and J.K.

DECLARATION OF INTERESTS

The authors declare no conflicts of interest.

SUPPLEMENTAL INFORMATION

Supplemental information can be found online at https://doi.org/10.1016/j.matt.2025.101988.

Received: August 21, 2024
Revised: November 27, 2024
Accepted: January 7, 2025
Published: February 10, 2025

REFERENCES

1. Nakatsuji, S., Kiyohara, N., and Higo, T. (2015). Large anomalous Hall effect in a non-collinear antiferromagnet at room temperature. Nature *527*, 212–215.
2. Nayak, A.K., Fischer, J.E., Sun, Y., Yan, B., Karel, J., Komarek, A.C., Shekhar, C., Kumar, N., Schnelle, W., Kübler, J., et al. (2016). Large anomalous Hall effect driven by a nonvanishing Berry curvature in the noncolinear antiferromagnet Mn_3Ge. Sci. Adv. *2*, e1501870.
3. Liu, Z.Q., Chen, H., Wang, J.M., Liu, J.H., Wang, K., Feng, Z.X., Yan, H., Wang, X.R., Jiang, C.B., Coey, J.M.D., and MacDonald, A.H. (2018). Electrical switching of the topological anomalous Hall effect in a non-collinear antiferromagnet above room temperature. Nat. Electron. *1*, 172–177.
4. Feng, Z., Zhou, X., Šmejkal, L., Wu, L., Zhu, Z., Guo, H., González-Hernández, R., Wang, X., Yan, H., Qin, P., et al. (2022). An anomalous Hall effect in altermagnetic ruthenium dioxide. Nat. Electron. *5*, 735–743.
5. Reichlova, H., Lopes Seeger, R., González-Hernández, R., Kounta, I., Schlitz, R., Kriegner, D., Ritzinger, P., Lammel, M., Leiviskä, M., Birk Hellenes, A., et al. (2024). Observation of a spontaneous anomalous Hall response in the Mn_5Si_3 d-wave altermagnet candidate. Nat. Commun. *15*, 4961.
6. Suzuki, T., Chisnell, R., Devarakonda, A., Liu, Y.-T., Feng, W., Xiao, D., Lynn, J.W., and Checkelsky, J. (2016). Large anomalous Hall effect in a half-Heusler antiferromagnet. Nat. Phys. *12*, 1119–1123.
7. Zeng, Q., Sheng, H., Ding, Y., Wang, L., Yang, W., Jiang, J.-Z., Mao, W.L., and Mao, H.-K. (2011). Long-range topological order in metallic glass. Science *332*, 1404–1406.
8. Luo, W.K., Sheng, H.W., Alamgir, F.M., Bai, J.M., He, J.H., and Ma, E. (2004). Icosahedral short-range order in amorphous alloys. Phys. Rev. Lett. *92*, 145502.
9. Streubel, R., Bouma, D.S., Bruni, F., Chen, X., Ercius, P., Ciston, J., N'Diaye, A.T., Roy, S., Kevan, S.D., Fischer, P., and Hellman, F. (2021). Chiral Spin Textures in Amorphous Iron–Germanium Thick Films. Adv. Mater. *33*, 2004830.
10. Yu, X.Z., Kanazawa, N., Onose, Y., Kimoto, K., Zhang, W.Z., Ishiwata, S., Matsui, Y., and Tokura, Y. (2011). Near room-temperature formation of a skyrmion crystal in thin-films of the helimagnet FeGe. Nat. Mater. *10*, 106–109.
11. Mitchell, N.P., Nash, L.M., Hexner, D., Turner, A.M., and Irvine, W.T.M. (2018). Amorphous topological insulators constructed from random point sets. Nat. Phys. *14*, 380–385.
12. Karel, J., Bouma, D.S., Fuchs, C., Bennett, S., Corbae, P., Song, S.B., Zhang, B.H., Wu, R.Q., and Hellman, F. (2020). Unexpected dependence of the anomalous Hall angle on the Hall conductivity in amorphous transition metal thin films. Phys. Rev. Mater. *4*, 114405.
13. Bouma, D.S., Chen, Z., Zhang, B., Bruni, F., Flatté, M.E., Ceballos, A., Streubel, R., Wang, L.-W., Wu, R.Q., and Hellman, F. (2020). Itinerant ferromagnetism and intrinsic anomalous Hall effect in amorphous iron-germanium. Phys. Rev. B *101*, 014402.
14. Fujiwara, K., Kato, Y., Abe, H., Noguchi, S., Shiogai, J., Niwa, Y., Kumigashira, H., Motome, Y., and Tsukazaki, A. (2023). Berry curvature contributions of kagome-lattice fragments in amorphous Fe–Sn thin films. Nat. Commun. *14*, 3399.
15. Tang, P., Zhou, Q., and Zhang, S.-C. (2017). Multiple types of topological fermions in transition metal silicides. Phys. Rev. Lett. *119*, 206402.
16. Sanchez, D.S., Belopolski, I., Cochran, T.A., Xu, X., Yin, J.-X., Chang, G., Xie, W., Manna, K., Süß, V., Huang, C.-Y., et al. (2019). Topological chiral crystals with helicoid-arc quantum states. Nature *567*, 500–505.
17. Rao, Z., Li, H., Zhang, T., Tian, S., Li, C., Fu, B., Tang, C., Wang, L., Li, Z., Fan, W., et al. (2019). Observation of unconventional chiral fermions with long Fermi arcs in CoSi. Nature *567*, 496–499.
18. Molinari, A., Balduini, F., Rocchino, L., Wawrzyńczak, R., Sousa, M., Bui, H., Lavoie, C., Stanic, V., Jordan-Sweet, J., Hopstaken, M., et al. (2023). Disorder-Induced Magnetotransport Anomalies in Amorphous and Textured $Co_{1-x}Si_x$ Semimetal Thin Films. ACS Appl. Electron. Mater. *5*, 2624–2637.
19. Belopolski, I., Manna, K., Sanchez, D.S., Chang, G., Ernst, B., Yin, J., Zhang, S.S., Cochran, T., Shumiya, N., Zheng, H., et al. (2019). Discovery of topological Weyl fermion lines and drumhead surface states in a room temperature magnet. Science *365*, 1278–1281.
20. Sakai, A., Mizuta, Y.P., Nugroho, A.A., Sihombing, R., Koretsune, T., Suzuki, M.-T., Takemori, N., Ishii, R., Nishio-Hamane, D., Arita, R., et al. (2018). Giant anomalous Nernst effect and quantum-critical scaling in a ferromagnetic semimetal. Nat. Phys. *14*, 1119–1124.
21. Manna, K., Muechler, L., Kao, T.-H., Stinshoff, R., Zhang, Y., Gooth, J., Kumar, N., Kreiner, G., Koepernik, K., Car, R., et al. (2018). From colossal to zero: controlling the anomalous Hall effect in magnetic Heusler compounds via Berry curvature design. Phys. Rev. X *8*, 041045.
22. Reichlova, H., Schlitz, R., Beckert, S., Swekis, P., Markou, A., Chen, Y.-C., Kriegner, D., Fabretti, S., Hyeon Park, G., Niemann, A., et al. (2018). Large anomalous Nernst effect in thin films of the Weyl semimetal Co_2MnGa. Appl. Phys. Lett. *113*, 212405.
23. Zhang, Y., Yin, Y., Dubuis, G., Butler, T., Medhekar, N.V., and Granville, S. (2021). Berry curvature origin of the thickness-dependent anomalous Hall effect in a ferromagnetic Weyl semimetal. npj Quantum Mater. *6*, 17.
24. Park, G.-H., Reichlova, H., Schlitz, R., Lammel, M., Markou, A., Swekis, P., Ritzinger, P., Kriegner, D., Noky, J., Gayles, J., et al. (2020). Thickness dependence of the anomalous Nernst effect and the Mott relation of Weyl semimetal Co_2MnGa thin films. Phys. Rev. B *101*, 060406.
25. Han, J., McGoldrick, B.C., Chou, C.-T., Safi, T.S., Hou, J.T., and Liu, L. (2021). Current-induced switching of a ferromagnetic Weyl semimetal Co_2MnGa. Appl. Phys. Lett. *119*, 212409.
26. Safi, T.S., Chou, C.-T., Hou, J.T., Han, J., and Liu, L. (2022). Spin-generation in magnetic Weyl semimetal Co_2MnGa across varying degree of chemical order. Appl. Phys. Lett. *121*, 092404.
27. Tang, K., Wen, Z., Lau, Y.-C., Sukegawa, H., Seki, T., and Mitani, S. (2021). Magnetization switching induced by spin–orbit torque from Co_2MnGa magnetic Weyl semimetal thin films. Appl. Phys. Lett. *118*, 062402.

28. Aoki, M., Yin, Y., Granville, S., Zhang, Y., Medhekar, N.V., Leiva, L., Ohshima, R., Ando, Y., and Shiraishi, M. (2023). Gigantic Anisotropy of Self-Induced Spin-Orbit Torque in Weyl Ferromagnet Co_2MnGa. Nano Lett. *23*, 6951–6957.

29. Wang, J., Lau, Y.C., Zhou, W., Seki, T., Sakuraba, Y., Kubota, T., Ito, K., and Takanashi, K. (2022). Strain-Induced Large Anomalous Nernst Effect in Polycrystalline Co_2MnGa/AlN Multilayers. Adv. Electron. Mater. *8*, 2101380.

30. Uesugi, R., Higo, T., and Nakatsuji, S. (2023). Giant anomalous Nernst effect in polycrystalline thin films of the Weyl ferromagnet Co_2MnGa. Appl. Phys. Lett. *123*, 252401.

31. Hsu, C.-H., Karel, J., Roschewsky, N., Kleidermacher, H., Sayed, S., Cheema, S., Bouma, D., Hellman, F., and Salahuddin, S. (2022). Large spin-orbit torque generated by amorphous iron silicide. Preprint at arXiv. https://doi.org/10.48550/arXiv.2006.07786.

32. Zhao, J., Jiang, B., Yang, J., Wang, L., Shi, H., Tian, G., Li, Z., Liu, E., and Wu, X. (2023). Magnetotransport induced by anomalous Hall effect. Phys. Rev. B *107*, L060408.

33. Raquet, B., Viret, M., Sondergard, E., Cespedes, O., and Mamy, R. (2002). Electron-magnon scattering and magnetic resistivity in 3*d* ferromagnets. Phys. Rev. B *66*, 024433.

34. Graf, T., Felser, C., and Parkin, S.S. (2011). Simple rules for the understanding of Heusler compounds. Prog. Solid State Chem. *39*, 1–50.

35. Karel, J., Bordel, C., Bouma, D.S., de Lorimier-Farmer, A., Lee, H.J., and Hellman, F. (2016). Scaling of the anomalous Hall effect in lower conductivity regimes. Europhys. Lett. *114*, 57004.

36. Bouma, D.S., Chen, Z., Zhang, B., Bruni, F., Flatté, M.E., Ceballos, A., Streubel, R., Wang, L.W., Wu, R.Q., and Hellman, F. (2020). Itinerant ferromagnetism and intrinsic anomalous Hall effect in amorphous iron-germanium. Phys. Rev. B *101*, 014402.

37. Ido, H., and Yasuda, S. (1988). Magnetic properties of Co-Heusler and related mixed alloys. J. Phys. Colloq. *49*, C8-C141–C8-142.

38. Yamane, K., Higo, Y., Uchida, H., Nanba, Y., Sasaki, S., Ohmori, H., Bessho, K., and Hosomi, M. (2013). Spin torque switching of perpendicularly magnetized CoFeB-based tunnel junctions with high thermal tolerance. IEEE Trans. Magn. *49*, 4335–4338.

39. Pai, C.-F. (2018). Switching by topological insulators. Nat. Mater. *17*, 755–757.

40. Pan, Q., Liu, Y., Wu, H., Zhang, P., Huang, H., Eckberg, C., Che, X., Wu, Y., Dai, B., Shao, Q., and Wang, K.L. (2022). Efficient Spin-Orbit Torque Switching of Perpendicular Magnetization using Topological Insulators with High Thermal Tolerance. Adv. Electron. Mater. *8*, 2200003.

41. Kudryavtsev, Y.V., Oksenenko, V.A., Lee, Y.P., Hyun, Y.H., Kim, J.B., Park, J.S., Park, S.Y., and Dubowik, J. (2007). Evolution of the magnetic properties of Co_2Mn Ga Heusler alloy films: From amorphous to ordered films. Phys. Rev. B *76*, 024430.

42. Kandpal, H.C., Fecher, G.H., and Felser, C. (2007). Calculated electronic and magnetic properties of the half-metallic, transition metal based Heusler compounds. J. Phys. D Appl. Phys. *40*, 1507–1523.

43. Qin, P., Yan, H., Wang, X., Chen, H., Meng, Z., Dong, J., Zhu, M., Cai, J., Feng, Z., Zhou, X., et al. (2023). Room-temperature magnetoresistance in an all-antiferromagnetic tunnel junction. Nature *613*, 485–489.

44. Karel, J., Bernardi, F., Wang, C., Stinshoff, R., Born, N.-O., Ouardi, S., Burkhardt, U., Fecher, G.H., and Felser, C. (2015). Evidence for localized moment picture in Mn-based Heusler compounds. Phys. Chem. Chem. Phys. *17*, 31707–31714.

45. Kresse, G., and Furthmüller, J. (1996). Efficiency of ab-initio total energy calculations for metals and semiconductors using a plane-wave basis set. Comput. Mater. Sci. *6*, 15–50.

46. Perdew, J.P., Burke, K., and Ernzerhof, M. (1996). Generalized gradient approximation made simple. Phys. Rev. Lett. *77*, 3865–3868.

47. Wu, Q., Zhang, S., Song, H.-F., Troyer, M., and Soluyanov, A.A. (2018). WannierTools: An open-source software package for novel topological materials. Comput. Phys. Commun. *224*, 405–416.

48. Wang, X., Yates, J.R., Souza, I., and Vanderbilt, D. (2006). Ab initio calculation of the anomalous Hall conductivity by Wannier interpolation. Phys. Rev. B *74*, 195118.

49. Xiao, D., Yao, Y., Fang, Z., and Niu, Q. (2006). Berry-phase effect in anomalous thermoelectric transport. Phys. Rev. Lett. *97*, 026603.

50. Wang, X., Vanderbilt, D., Yates, J.R., and Souza, I. (2007). Fermi-surface calculation of the anomalous Hall conductivity. Phys. Rev. B *76*, 195109.

51. Mostofi, A.A., Yates, J.R., Lee, Y.-S., Souza, I., Vanderbilt, D., and Marzari, N. (2008). wannier90: A tool for obtaining maximally-localised Wannier functions. Comput. Phys. Commun. *178*, 685–699.